RSC Advances

PAPER

View Article Online
View Journal | View Issue

Cite this: *RSC Adv.*, 2024, **14**, 4252

Activated carbon from *Camellia oleifera* shells for adsorption of Y(III): experimental and DFT studies

Bin Zeng,[abc] Xiangrong Zeng, *[ac] Lianghui Hu,[c] Lijinhong Huang,*[bd] Yuxiang Huang,[a] Yi Zhou,[a] Guoliang Liu[a] and Wanfu Huang[b]

Received 12th December 2023
Accepted 18th January 2024

DOI: 10.1039/d3ra08487f

rsc.li/rsc-advances

Yttrium is an important rare earth element and is widely used in fields such as special glass preparation, metallurgy, and materials science. However, it is difficult to recover yttrium ion waste from dilute solutions with traditional processes, resulting in a significant waste of rare earth resources. The simple, effective, and easy-to-operate adsorption method is the most promising method for recovering yttrium, which is of great significance for sustainable development of the rare earth industry. In this study, activated carbon was prepared from *Camellia oleifera* fruit shells (COS) using phosphoric acid activation, and efficient recovery of Y(III) from the *Camellia oleifera* fruit shell activated carbon was studied. Adsorption equilibrium data showed that this activated carbon had a Y(III) adsorption capacity of 35.41 mg g^{-1}, indicating significant potential for recovery of yttrium ions. The adsorption of Y(III) by the activated carbon prepared from COS was consistent with the Langmuir model, and the adsorption data were consistent with the pseudo second-order kinetic model, indicating that the adsorption process was primarily chemical adsorption. After adsorption, the surface of the activated carbon contained large amounts of N, O, and Y, indicating that Y(III) was stably adsorbed. The mechanisms for adsorption of Y(III) on three types of activated carbon were studied through DFT calculations. The results showed that Y(III) interacted with the carbon atoms on the surfaces to form new chemical bonds. The yttrium ion adsorption capacities for the three different activated carbons decreased in the order C I > C II > C.

1. Introduction

The rare earth elements include the 15 lanthanide elements (from La to Lu) plus scandium (Sc) and yttrium (Y).[1,2] They play an important role in manufacturing advanced materials and are widely used in sensing materials, luminescent materials, nanomaterials, battery components,[3] permanent magnets,[4] and superconducting materials. Yttrium is an important rare earth element[5] and is used in fields such as special glass preparation,[6] metallurgy,[7] and materials science.[8] As a nonrenewable rare earth, the scale of yttrium use has continuously been reduced by extensive development and utilization.[9] According to statistics, mining wastewater (including coal mine drainage) contains a large amount of low concentration rare earth ions, which have been explored as an attractive secondary source for rare earth recovery.[10] However, it is difficult to recover rare earth waste from dilute solutions *via* traditional processes, resulting in a significant waste of rare earth resources.[11] Therefore, the recovery of valuable rare earth elements such as yttrium from dilute rare earth wastewater solutions is of great significance for sustainable development of the rare earth industry.

Researchers have developed several technologies for recovering the rare earths from wastewater, including biological methods,[12] chemical precipitation,[13] solvent extraction,[14,15] membrane filtration, electrodialysis, and adsorption.[16] Due to the cost-effectiveness and environmental friendliness of adsorption materials, recycling and utilization of the rare earths in wastewater has attracted much attention.[17,18] Currently, the research on rare earth adsorption materials includes zeolites, clays,[19,20] resins, activated carbon, *etc.*[21] Due to the low concentrations of rare earths in wastewater,[22] the ion adsorption materials used in recovering them must have high adsorption capacities, fast adsorption processes, high selectivities, and high enrichment efficiencies. It is difficult to meet these requirements with the currently used adsorption materials.

Camellia oleifera is widely planted and is one of the four major woody oil tree species in the world.[23,24] The yield of *Camellia oleifera* fruit husks is high, but the utilization rate is low.[25] According to statistics, over 3.0×10^6 tons of COS are discarded or burned per year,[26] which constitutes a waste of resources and environmental pollution.[27,28] The main components of COS are lignin, hemicellulose, and cellulose,[29] which

[a]*Gannan University of Science and Technology, Ganzhou 341000, China. E-mail: zengxr986@163.com*

[b]*Jiangxi University of Science and Technology, Ganzhou 341000, China. E-mail: angeline777@sina.com*

[c]*Jiangxi Yaosheng Tungsten Industry Co., Ltd, Ganzhou 341000, China*

[d]*WA School of Mines: Minerals, Energy and Chemical Engineering, Curtin University, Perth WA 6845, Australia*

are excellent precursor materials for carbon production.[30] Research has shown that the carbon prepared from COS adsorbs toxic chemicals[31,32] and harmful heavy metal ions such as lead, cadmium, and copper in aqueous solutions.[33] Therefore, the shells of *Camellia oleifera* have become a promising alternative raw material for producing activated carbon due to the high yield and low cost. Research on preparing high-performance activated carbon from COS to adsorb low concentrations of rare earth ions. Not only can a feasible treatment path be found for COS, but rare earth ions can also be recovered and environmentally friendly, achieving the goal of "treating waste with waste".

Therefore, this study used COS as the precursor raw material and optimized the phosphoric acid activation method to prepare high-performance COS activated carbon exhibiting a high recovery rate for the rare earth Y(III). This provides a theoretical reference for the application of *Camellia oleifera* shell activated carbon for adsorption of rare earths in wastewater.

2. Experimental

2.1. Materials and reagents

The shells of *Camellia oleifera* were used for the preparation of activated carbon and were collected from Ganzhou, Jiangxi, China. After washing with distilled water, the shells were dried at 105 °C for 24 h. Phosphoric acid was purchased from China National Pharmaceutical Group Chemical Reagent Co., Ltd. (Shanghai, China). All chemical reagents used in this study were of analytical reagent grade and were used without further purification. The water used in the experiment was deionized water.

2.2. Synthesis of activated carbon from COS

In the process for preparation of activated carbon for *Camellia oleifera* fruit husks, (1) the dried *Camellia oleifera* fruit husks were crushed with a stainless steel pulverizer to provide the required particle sizes; (2) five g of *Camellia oleifera* shell powder with the desired particle sizes was weighted and mixed with a certain proportion of phosphoric acid and soaked for a period; (3) the impregnated sample was transferred to a quartz boat and placed in a tube furnace. First, nitrogen gas was introduced to remove the air, and then the sample was heated to the desired temperature for 1 h. (4) After cooling to room temperature, the activated carbon was removed from the *Camellia oleifera* shells, washed with deionized water until the pH was constant, filtered and dried, and the dried sample was screened to 100 mesh.

2.3. Characterization of the activated carbon from COS

X-ray photoelectron spectroscopy (Thermo Scientific K-Alpha, USA) with an Al Kα source was used to detect the surface binding state and elemental morphology of the activated carbon. The surface morphologies and energy spectra of the raw materials and activated carbon were examined with a scanning electron microscope (ZEISS Sigma 300 from Germany). An inductively coupled plasma emission spectrometer (ICP-OES, France) was used to detect the Y^{3+} concentrations with the manufacturer's recommended instrumental parameters.

2.4. Adsorption experiments

Y(III) ion solutions were prepared with different concentrations of $Y(NO_3)_3 \cdot 6H_2O$ for adsorption experiments. Ten milligrams of sample was added to give 25 mL of the Y(III) solution for the batch adsorption experiments. The adsorption experiments were conducted in a constant temperature oscillator operated at 150 rpm for different durations. After completion of the experiment, the volume was measured following filtration through a 0.45 μm filter membrane, and the concentration of yttrium ions was determined. Duplicate samples were prepared for each experiment. All results were the average of duplicate samples, with relative errors of less than 5%.

2.5. Kinetic and isothermal models

The pseudo first-order kinetic model and pseudo second-order kinetic model were used for data fitting and analyses with eqn (1) and (2) to determine the rate-controlling steps for Y^{3+} adsorption on carbon samples:[34,35]

$$\ln(q_e - q_t) = \ln q_e - k_1 t \quad (1)$$

$$\frac{t}{q_t} = \frac{1}{k_2 q_e^2} + \frac{1}{q_e} t \quad (2)$$

where q_e and q_t are the adsorption equilibrium and adsorption capacity of Y^{3+} at time t (mg g^{-1}), respectively, t is the contact time (min), and k_1 and k_2 are the pseudo first-order and pseudo second-order rate constants, respectively.

The Langmuir model and Freundlich model were used for fitting and analyses to study the interactions between the activated carbon and the adsorbate. These two models were used to describe the electroadsorption process and the maximum adsorption capacity:[36]

$$q_e = \frac{q_m K_L C_e}{1 + K_L C_e} \quad (3)$$

$$\ln q_e = \ln K_F + \frac{1}{n} \ln C_e \quad (4)$$

where q_e and q_m are the adsorption capacity and the maximum adsorption capacity (mg g^{-1}), respectively, at adsorption equilibrium; C_e is the concentration of adsorbate in solution at equilibrium (mg L^{-1}); K_L is the Langmuir constant (L mg^{-1}); and K_F is the Freundlich constant. $\frac{1}{n}$ is the Freundlich exponent.

3. Results and discussion

3.1. Effects of preparation conditions for the activated carbon from COS on Y(III) adsorption

The granularity, soaking time, soaking ratio (mL H_3PO_4 per g COS) and activation temperature were the key parameters used in preparing the camellia shell-derived activated carbon, and they affected the Y(III) adsorption performance. To prepare

highly efficient activated carbon from the COS, we studied the effects of the preparation conditions on COS adsorption.

The effect of the particle size on the performance of the activated carbon is shown in Fig. 1(a). When the particle size was −0.106 mm, the COS activated carbon exhibited the highest efficiency for adsorption of Y(III), with an adsorption capacity of 19.55 mg g^{-1}. The particle sizes had a significant impact on the activated carbon from the COS, and as the particle sizes decreased, the efficiency of Y(III) adsorption increased. The reason for this may be that as the particle sizes decreased, more micropores were formed in activated carbon, which facilitated the adsorption of Y(III). Therefore, the optimal particle sizes of −0.106 mm was used to prepare the activated carbon from the COS.

To investigate the effect of impregnation time on the adsorption capacities for the rare earth ions, activated carbons were prepared with different impregnation times (0, 2, 3, 6, 12 h) while other parameters remained unchanged. As shown in Fig. 1(b), the Y(III) adsorption capacity was rapidly increased when the soaking time was increased from 1 h to 2 h, reaching its maximum value of 19.55 mg g^{-1} at approximately 2 h. When the time was increased further to 12 h, the Y(III) adsorption capacity decreased slowly. This may have occurred because hydrolysis of the lignin in the COS with phosphoric acid was enhanced as the soaking time increased, which formed more micropores in the activated carbon. However, longer time mays may have led to excessive erosion of the carbon body and reduced the performance. Therefore, the optimal soaking time of 2 h was used to study the effect of the soaking ratio on the adsorption capacity of the activated carbon.

To investigate the effect of the impregnation ratio on the adsorption capacities of rare earth ions, activated carbon preparation experiments were conducted with different impregnation ratios while the other parameters remained unchanged. As shown in Fig. 1(c), when the impregnation ratio (mL phosphoric acid per g COS) was increased from 7.5 : 5 to 17.5 : 5, the efficiency for Y(III) adsorption on the activated carbon first increased and then decreased. When the impregnation ratio was increased from 7.5 : 5 to 12.5 : 5, the Y(III) adsorption capacity rapidly increased and reached the maximum of 19.55 mg g^{-1} at approximately 12.5 : 5. As time was increased further to 17.5 : 5, the capacity for Y(III) adsorption on the activated carbon decreased. Therefore, the optimal impregnation ratio was 12.5 : 5.

To investigate the effect of the activation temperature on the adsorption capacities of rare earth ions, experiments were conducted with activated carbons prepared at different activation temperatures (300 °C, 400 °C, 500 °C, 600 °C, 700 °C), while other parameters remained unchanged. Fig. 1(d) shows that with increasing activation temperature, the Y(III) adsorption capacity increased. When the activation temperature was increased from 300 °C to 600 °C, the capacity for Y(III) adsorption increased from 8.35 mg g^{-1} to 35.41 mg g^{-1}. As the temperature was increased to 700 °C, the Y(III) adsorption

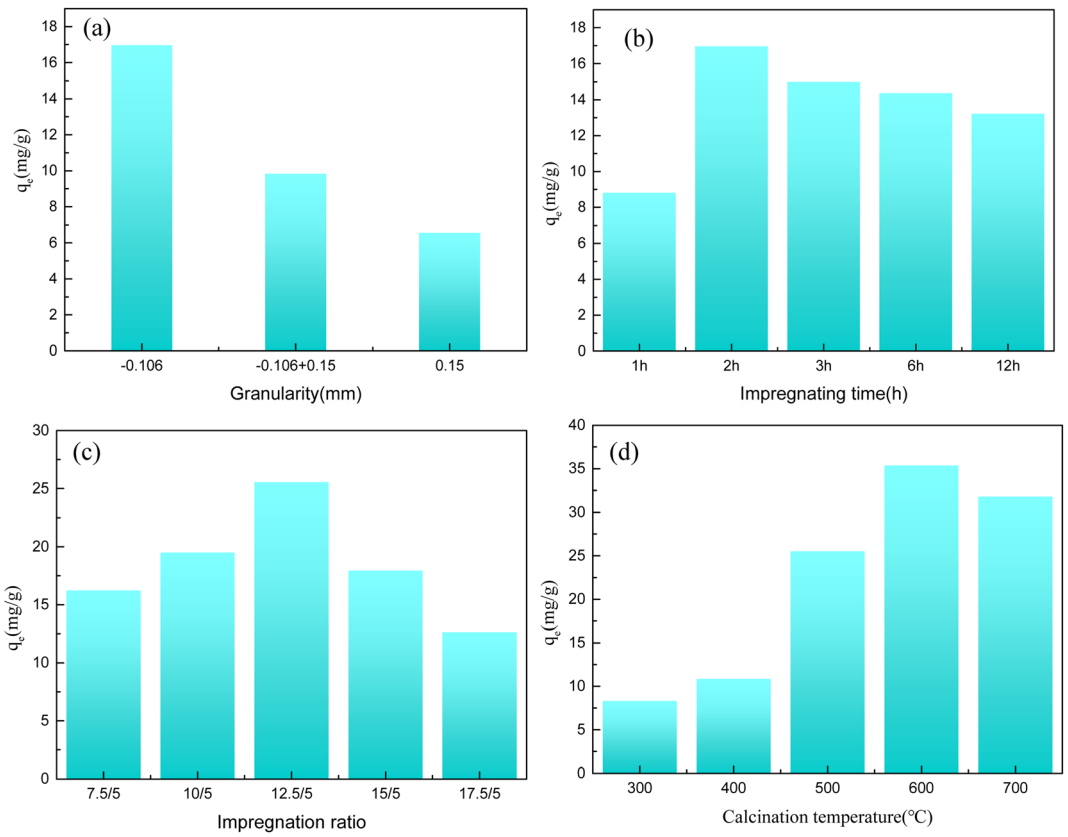

Fig. 1 Effects of (a) the particle size, (b) impregnation times, and (c) impregnation ratio, (d) activation temperature on Y(III) adsorption.

capacity decreased to 31.87 mg g^{-1}. Therefore, after considering the activation temperature carefully, 600 °C was chosen.

3.2. Kinetics and isotherms

The activated carbon was prepared from the COS with a soaking time of 2 h, a soaking ratio of 12.5 : 5, and an activation temperature of 600 °C. The amounts of Y(III) adsorbed on the activated carbon with different initial concentration conditions were studied to explore the adsorption performance and mechanism. The capacity for Y(III) adsorption on the activated carbons with different contact times was studied to determine the main steps controlling the adsorption process.

The effect of contact time on the adsorption performance of the activated carbon prepared from the COS is shown in Fig. 2(a). With increasing time, the adsorption capacity of activated carbon from the COS for Y(III) rapidly increased, reaching 90% of the maximum adsorption capacity within 30 minutes. As the time was increased further, the growth rate slowed and equilibrium was reached after 120 minutes, at which point the adsorption capacity for Y(III) was 35.41 mg g^{-1}. The effect of different rare earth ion initial concentrations on adsorption by the activated carbon from the COS was also studied. As shown in Fig. 2(b), as the initial concentration of Y(III) was increased from 30 mg L^{-1} to 200 mg L^{-1}, the Y(III) adsorption capacity increased from 22.39 mg g^{-1} to 35.41 mg g^{-1}. As the initial concentration was increased to 200 mg L^{-1}, the growth rate for the adsorption capacity slowed, and adsorption gradually approached equilibrium.

Nonlinear fitting was applied to the adsorption data with pseudo first-order and pseudo second-order kinetic models to explore the Y(III) adsorption on the activated carbon from the COS. The resulting fitting curves were drawn, as shown in Fig. 3(a) and (b). The adsorption data were fitted with the Langmuir model and the Freundlich model to evaluate the mechanism for adsorption of Y(III) on the activated carbon. The fits for the Langmuir model and Freundlich model are shown in Fig. 3(c) and (d).

Fig. 3(a) and (b) shows that, compared with the pseudo first-order kinetic model, the pseudo second-order kinetic model provided a better fit with the adsorption data, and the correlation coefficient was greater than 0.99. Therefore, it can be concluded that the adsorption of Y(III) on the activated carbon from *Camellia oleifera* fruit shells primarily involved chemical adsorption. Fig. 3(c) and (d) shows that the correlation coefficient for the Langmuir model was 0.99, which was higher than the correlation coefficient of the Freundlich model, 0.93. This indicated that the adsorption of Y(III) on the activated carbon was more consistent with the Langmuir model. Therefore, the adsorption of Y(III) by the activated carbon from the COS primarily involved monolayer adsorption.

3.3. XPS analyses of the activated carbon from the COS

XPS analyses of the activated carbons prepared at different temperatures were used to understand the effect of temperature on the amounts of oxygen and nitrogen functional groups present on the surface of the material.

Fig. 4 show that the temperature significantly affected the surface oxygen, phosphorus, and nitrogen functional groups present on the activated carbon from the COS. As the temperature was increased with the range 400 °C to 600 °C, the N 1s peak for the activated carbon increased significantly, while the O 1s peak was significantly weakened. Table 1 show that when the temperature was increased from 400 °C to 500 °C, the N content increased from 1.06% to 1.23%, and the O content decreased from 10.93% to 7.75%, indicating the presence of P. When the temperature was further increased to 500 °C, the N content increased to 1.69%, and the O content decreased to 6.52%. At this time, the proportion of P was 0.6%. This indicated that the increased temperatures increased the proportions of N-containing functional groups and P-containing functional groups on the surface of activated carbon but reduced the proportion of O-containing functional groups, which improved the rare earth ion adsorption capacities of the activated carbon from the COS.

3.4. SEM-EDS analyses of Y(III) adsorption on activated carbon from the COS

SEM-EDS was used to analyse the surface morphology and elemental distribution of the activated carbon after adsorption of Y(III) to determine whether the activated carbon prepared

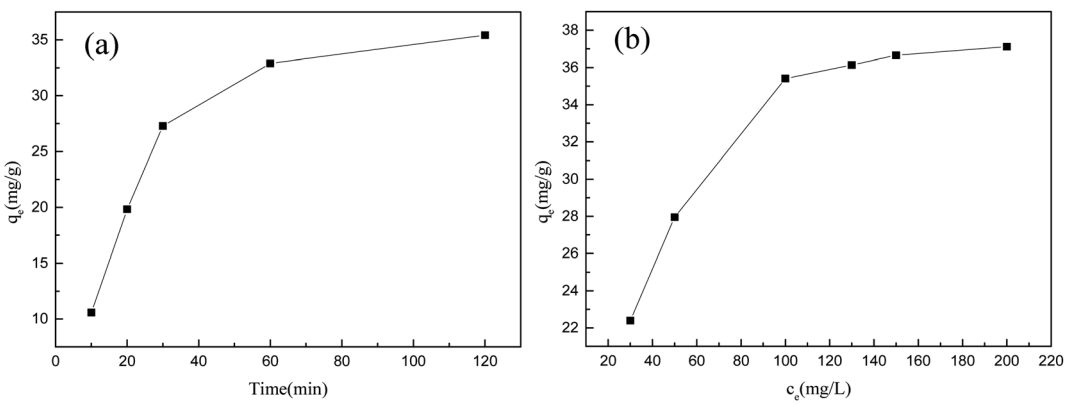

Fig. 2 (a) Kinetics and (b) isotherms for La^{3+} adsorption on activated carbon from the COS.

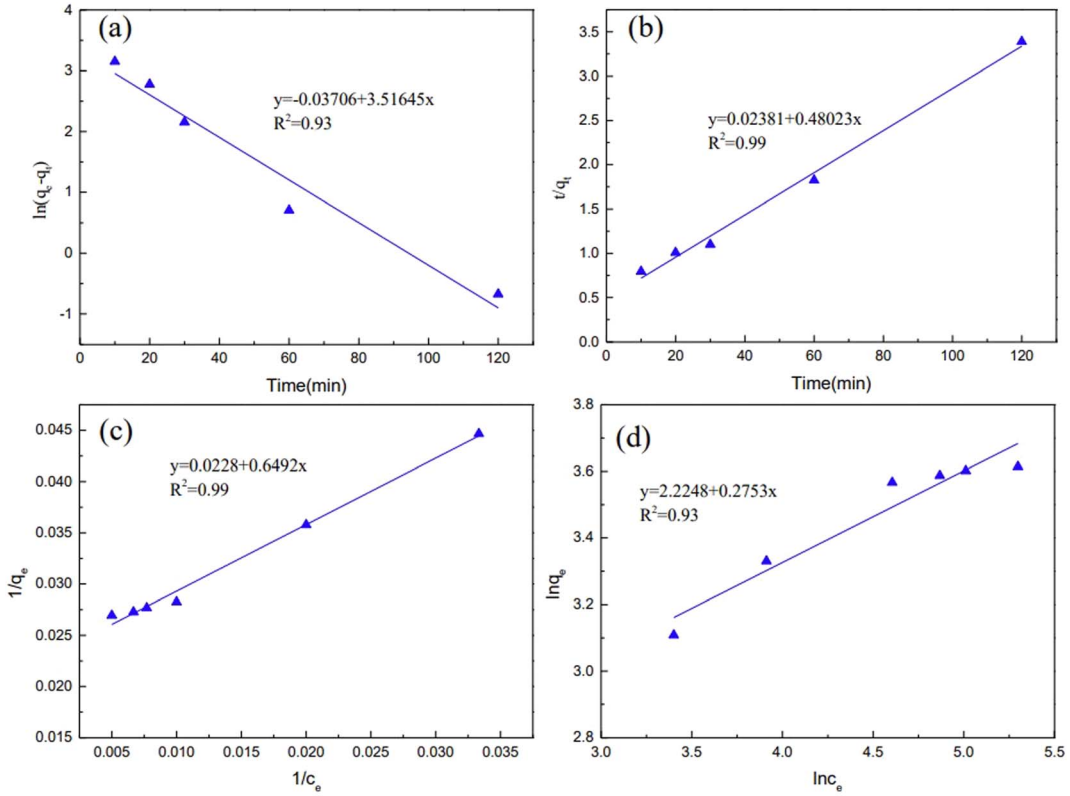

Fig. 3 Kinetics and isotherm fitting curves ((a): pseudo first-order dynamic model; (b): pseudo second-order dynamic model; (c): Langmuir model; (d): Freundlich model).

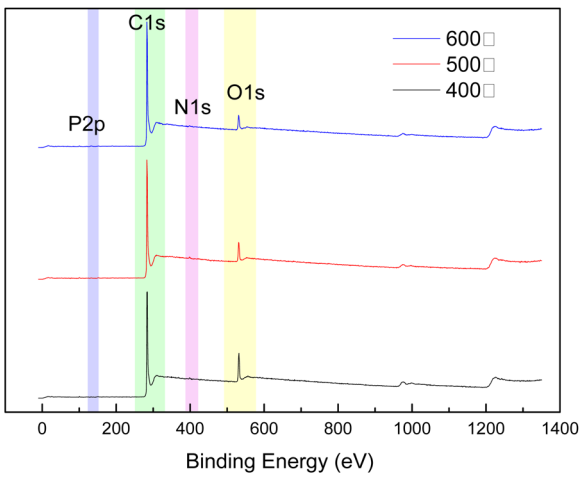

Fig. 4 XPS analyses of activated carbons prepared at different temperatures.

Table 1 Proportions of C, N, P, and O seen at different temperatures

Temperature	C (%)	N (%)	P (%)	O (%)
400 °C	88.01	1.06	0	10.93
500 °C	91.02	1.23	0	7.75
600 °C	91.19	1.69	0.60	6.52

from the COS captured Y(III) efficiently. Fig. 5 shows that the activated carbon had a porous structure; the surface contained large amounts of C, N, O, and P, and yttrium was also detected.

3.5. Adsorption capacity

To evaluate the practical application value of COS for Y(III) recovery, Table 2 summarizes the maximum adsorption capacity (reported in mg g^{-1}) of other adsorbents for Y(III). Compared with other adsorbents reported in the literature, COS have higher adsorption performance and great potential in Y(III) recovery.

3.6. DFT study on the adsorption of Y(III) by the activated carbon from the COS

Activated carbon comprises an accumulation of irregular and small graphene crystals. Magnetic resonance imaging (MRI) showed that the small graphene crystals were composed of several aromatic ring clustered together. Therefore, a single-layer graphene structure is frequently used to model carbon materials in quantum chemistry,[42] and good results have been obtained in those calculations.[43] Chen and Yang[44] found that graphene models composed of six or more benzene rings effectively simulated carbon-based materials. Because the activated carbon was irregularly formed,[45] two main surface defect structures were used herein to approximate the true structure of the activated carbon from the COS, and the optimized structure is shown in Fig. 6.

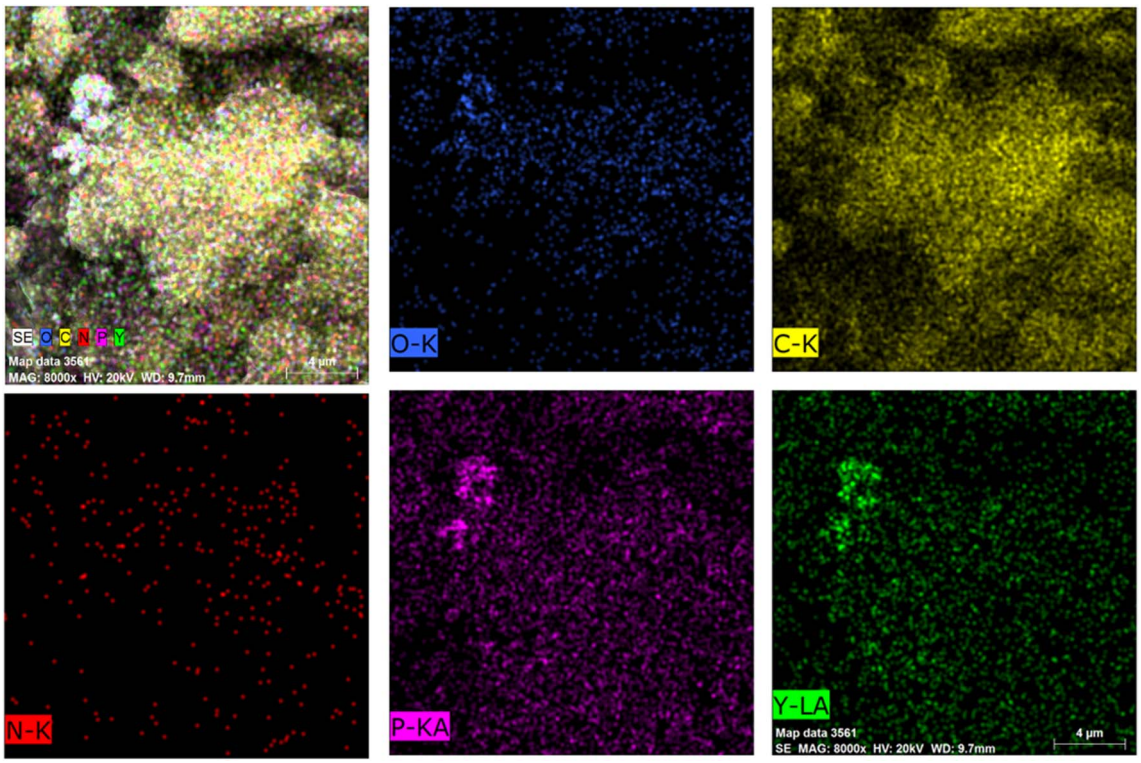

Fig. 5 Adsorption of Y(III) on the activated carbon from the COS.

Table 2 Adsorption capacity of different adsorbents for Y(III)

Sorbent	Max adsorption capacity (mg g^{-1})	Ref.
Cobalt iron oxide alginate nanocomposite	78.2	37
Fe_3O_4@SiO_2@polyaniline–graphene oxide	8.10	38
Graphene oxide–tris(4-aminophenyl) amine composites nanoparticles	10.52	39
Multiwalled carbon nanotubes	7.75	40
Fe_3O_4@TiO_2@P_20_4 nanoparticles	6.1	41
Nanometer-sized TiO_2	35.41	This study
COS		

3.6.1 Adsorption of Y(III) on the C-type activated carbon structure. Y(III) was placed on the adsorption sites of the C-type activated carbon surface for the calculations, and the results are shown in Fig. 7. After relaxation, the Y(III) ion was significantly closer to the surface of the activated carbon. Before adsorption, the distance between the Y(III) and the C atoms was outside the bonding range. After adsorption and stabilization, the farthest distance between the Y(III) and C4 was 2.7614 Å; the shortest distance, from C2, was 2.70666 Å. The calculations indicated that new chemical bonds were formed between the Y(III) ions and C1, C2, C3, C4, C5, and C7 on the surface of activated carbon. Therefore, the Y(III) ions were stably adsorbed on the carbon surface with the C-type structure.

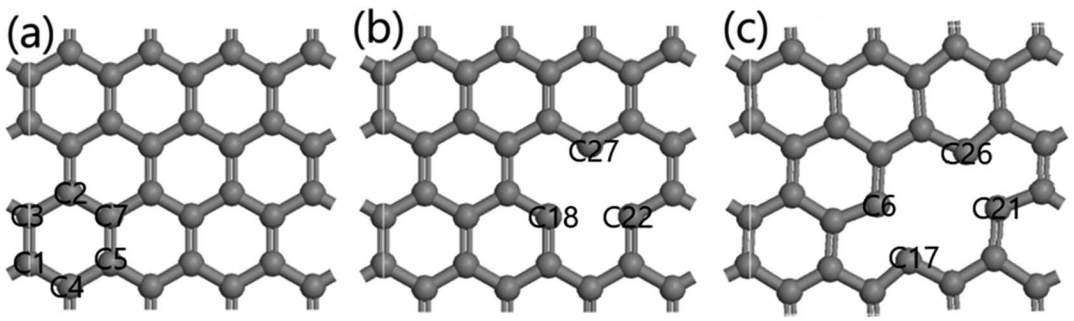

Fig. 6 Structure of the activated carbon prepared from the COS ((a) is the defect-free structure marked as C; (b and c) are the defect-activated carbon structures marked as C I and C II).

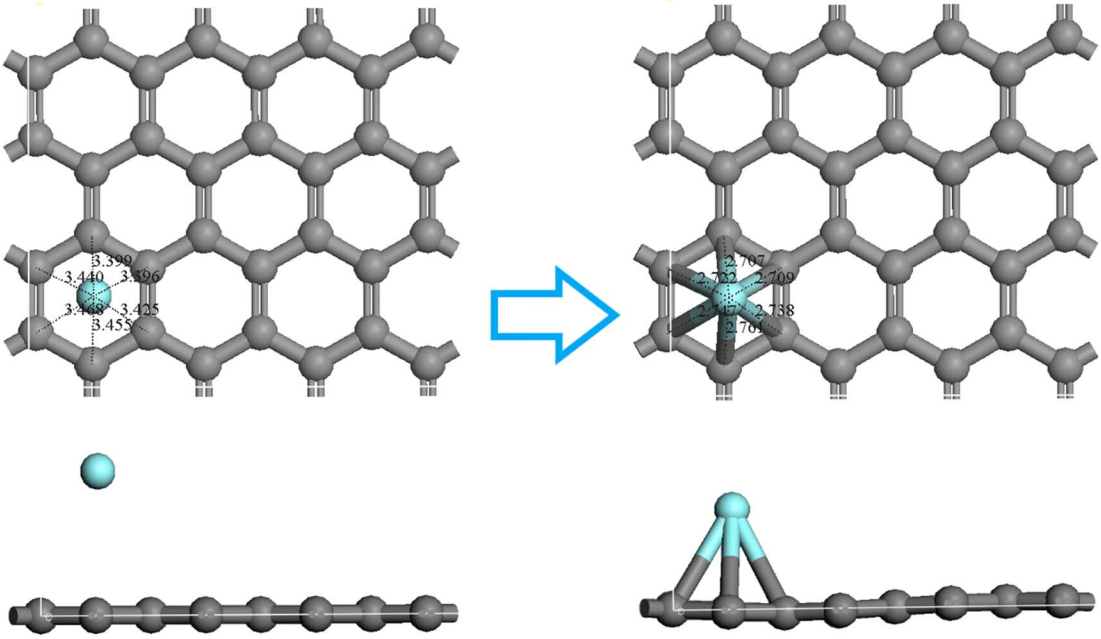

Fig. 7 Model for Y(III) before and after adsorption on the C-type surface.

To understand the mechanism for interaction between the Y(III) and the surface of the activated carbon further, we determined the density of states for the most stable adsorption configuration. Fig. 8 shows the partial wave density of states for C and Y after adsorption of the rare earth ion Y on the carbon surface. The 5 s orbitals of the Y ions were distributed within the range −1 to 7.5 eV at the bottom of the valence band and exhibited sharp peaks within the range −1 to 1.5 eV. The 4p orbitals of the Y ions were distributed within the range 1 to 10 eV at the bottom of the valence band and exhibited sharp

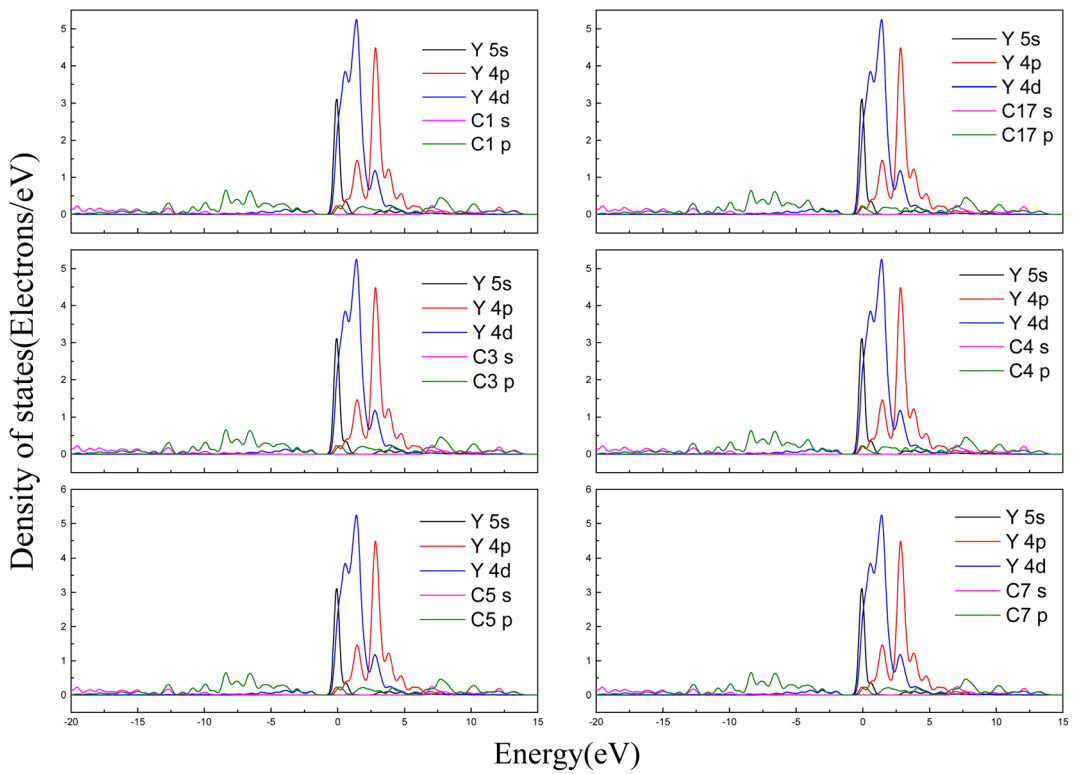

Fig. 8 Partial wave density of states for Y(III) after adsorption on a C-type surface.

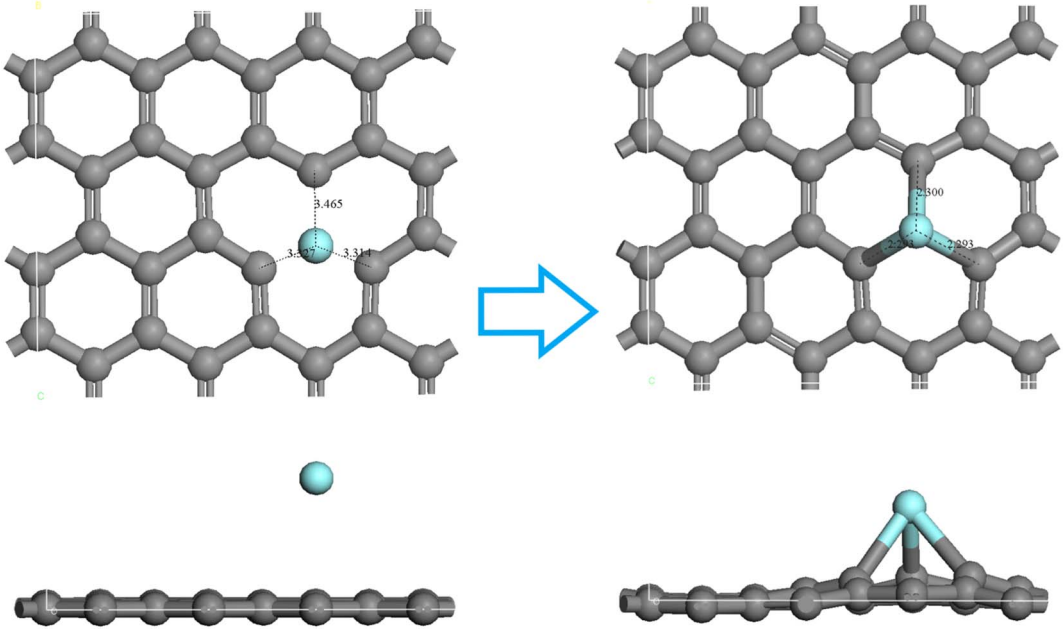

Fig. 9 Model for Y(III) before and after adsorption on the C I surface.

peaks within the ranges 2.5–3.5 eV and 1–2.5 eV. The 4d orbitals of the Y ions were distributed within the range −7.5 to 5 eV at the bottom of the valence band, and their highest peaks were within the range 1–2.5 eV and sharp peaks were found at −1 to 1 eV and 2.5–5 eV. The p orbitals of the C atoms were distributed within the range −15 to 17.5 eV, with multiple weak peaks present in the range −1 to −0.5 eV. The p orbitals of the C atom overlapped slightly with the 4d orbitals of the Y ions in the range −3 to −1.5 eV. Based on a comprehensive analysis of the bond populations results, the mechanism for adsorption of Y(III) on the C surface involved weak hybridization between the C atom p orbital and the Y ion 4d orbital on the surface.

3.6.2 Adsorption of Y(III) on the C I-type structure of the activated carbon. The adsorption calculation was performed by placing Y(III) at an adsorption site on the surface of the C I-type defect structure, and the results are shown in Fig. 9. After relaxation, the Y(III) was significantly closer to the surface of the activated carbon. Before adsorption, the distances between Y(III) and C18, C22, and C27 were 3.327 Å, 3.465 Å, and 3.334 Å, respectively, which were outside the bonding range. After adsorption stabilization, the distance between Y(III) and C18 changed from 3.327 Å to 2.495 Å, which reduced the distances from C22 and C27 to 2.293 Å and 2.29963 Å. The calculated adsorption structure indicated that the Y(III) on the surface of the activated carbon underwent bonding with C18, C22, and C27. Therefore, the rare earth Y(III) ion was stably adsorbed on the C surface with a type C I defect structure.

To further understand the interaction mechanism between Y(III) and the surface of the activated carbon, we calculated the density of states for the most stable adsorption configuration, as shown in Fig. 10. The 5s orbitals of the Y ions were distributed within the range −5 to 5 eV at the bottom of the valence band and exhibited sharp peaks at −3 to 2 eV, −0.5 to 0.5 eV,

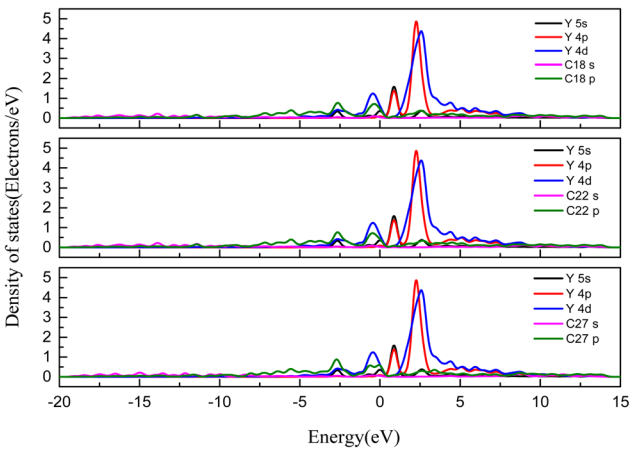

Fig. 10 Partial wave density of states for Y(III) adsorbed on the C I-type surface.

and 2–3 eV. The 4p orbitals of the Y ions were distributed in the range 0–10 eV at the bottom of the valence band and exhibited sharp peaks in the ranges 0–2 eV and 2–3 eV. The 4d orbitals of the Y ions were distributed within the range −5 to 10 eV at the bottom of the valence band, with sharp peaks at −3 to 2 eV, −2 to 1 eV, and −1.5 to 3 eV. The p orbitals of the C atoms exhibited sharp peaks within the ranges −2 to −1.5 eV, −1 to −0.5 eV, −7.5 to 10 eV, and 2–4 eV. The p orbitals of the C atom and the 4d orbitals of the Y ion overlapped significantly within the ranges −2 to 1.5 eV and −1 to 0.5 eV, and the 5s orbitals of the Y ions overlapped significantly within the ranges −3 to 2 eV, −0.5 to 0.5 eV, and 2–3 eV, resulting in significant hybridization. In summary, the mechanism for Y(III) adsorption on the surface of activated carbon involved hybridization of the C atom p orbitals

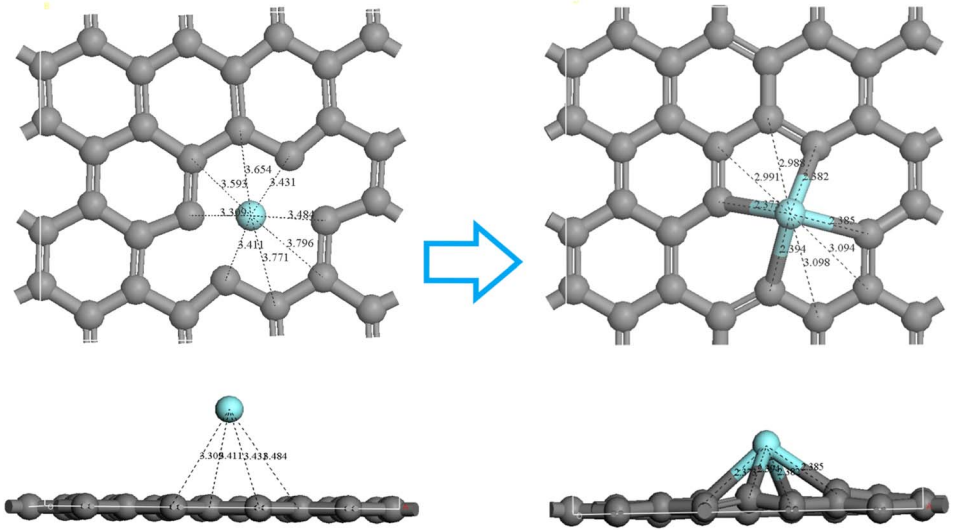

Fig. 11 Models for Y(III) before and after adsorption on the C II surface.

and the Y ion 5s and 4d orbitals on the surface, thereby forming stable chemical bonds.

3.6.3 Adsorption of Y(III) on the C II-type activated carbon structure. A Y(III) ion was placed at an adsorption site on the surface of the C II defect structure for to calculate the adsorption energy. Fig. 11 shows the changes of the Y(III) occurring after adsorption on the surface of the activated carbon: after relaxation, the Y(III) ion was significantly closer to the surface of the activated carbon. Before adsorption, the distances between Y(III) and C6, C17, C21, and C26 were 2.589 Å, 3.568 Å, 2.38478 Å, and 2.38231 Å, respectively, which were outside the bonding range. After adsorption and stabilization, the distances between Y(III) and C6, C17, C21, and C26 decreased to 2.37282 Å, 2.39354 Å, 2.38478 Å, and 2.38231 Å, respectively. The calculation of the surface indicated that the Y(III) on the activated carbon underwent bonding with C6, C17, C21, and C26. Therefore, the rare earth Y(III) was stably adsorbed on the C surface with the type II defect structure.

To understand the mechanism for the interaction between the Y(III) and the surface of the activated carbon, we calculated the density of states for the most stable adsorption configuration. Fig. 12 shows the partial wave density of states for C and Y after adsorption of the Y(III) on the carbon surface. The 5s orbitals of Y ions were distributed within the range −3 to 10 eV

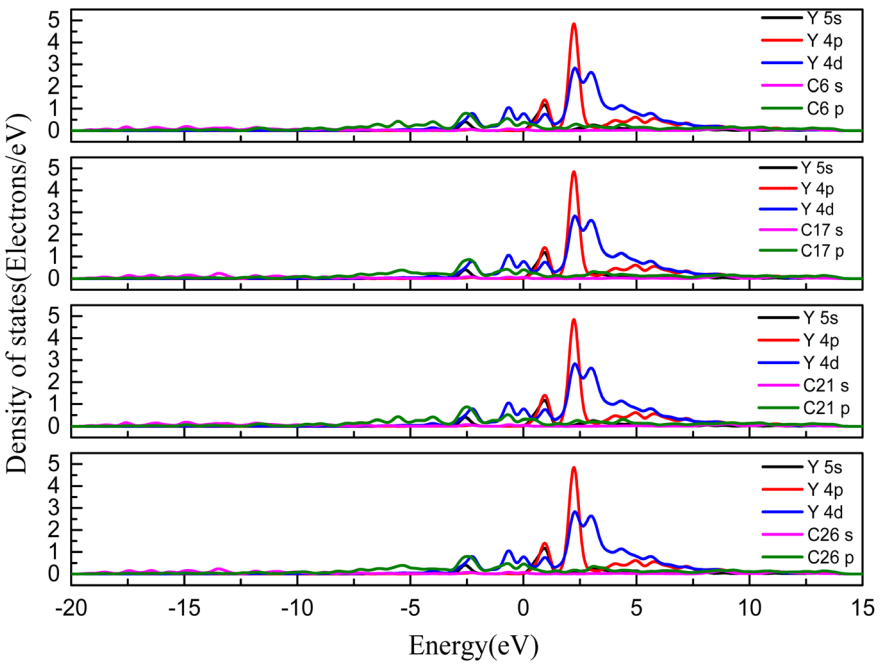

Fig. 12 Partial wave density of states for Y(III) adsorbed on the C II surface.

Table 3 Energies for adsorption of Y(III) on different activated carbon surfaces (units: eV)

Surface	Adsorbate	$E_{adsorbate/slab}$	$E_{adsorbate}$	E_{slab}	E_{ads}
C	Y	−5152.9	−4963.27	−188.51	−1.12
C 1	Y	−4994.22	−4800.04	−188.51	−5.67
C II	Y	−4838.42	−4644.72	−188.51	−5.19

at the bottom of the valence band, with sharp peaks at −3 to 2 eV and 0–2 eV and weak peaks at 3–4 eV and 8–9 eV. The 4p orbitals of the Y ion were distributed within the range 0–10 eV at the bottom of the valence band and showed the highest peak within the range of 2–3 eV, followed by a subpeak within the range 0.2–2 eV and a long and wide peak within the range 3–7.5 eV. The 4d orbitals of Y were distributed within the range 3 to 9 eV at the bottom of the valence band, and there were three strong peaks within the range 2 to 4 eV, appearing as peaks at −3 to 2 eV, −1 to −0.2 eV, and 0.5 to 1.8 eV. The p orbitals of the C atoms were distributed within the range −8 to 10 eV, exhibiting sharp peaks within the range −2.8 to −2 eV, multiple peaks within the range −1.8 to 0.5 eV, and weak, broad peaks within the range 2–5 eV and 2–4 eV. The p orbitals of the C atoms overlapped significantly with the 4d orbitals of the Y ion within the ranges −2.8 to −2 eV and −1.8 to −0.5 eV, and the 5s orbitals of the Y ion overlapped significantly within the ranges −2.8 to −2.3 eV and −0.3 to 1.8 eV. The 4p orbitals of the Y ion overlapped significantly within the range −0.3 to 1.8 eV, indicating significant hybridization between the p orbitals of the C atom and the 5s, 4p, and 4d orbitals of the Y ion. In summary, the mechanism for Y(III) adsorption on the surface of the activated carbon involved hybridization of the C p orbitals on the surface with the 5s and 4d orbitals of Y ions, thereby forming stable chemical bonds.

3.6.4 Analysis of the Y(III) adsorption energy on different activated carbon surfaces. Adsorption energy calculations were conducted to determine the strengths of Y(III) adsorption on the different activated carbon surfaces, and the results are shown in Table 3. The energies for adsorption of Y(III) on the C, C I, and C II surfaces were −1.12 eV, −5.67 eV, and −5.19 eV, respectively, indicating that Y(III) was stably adsorbed on the surfaces of the activated carbons, mainly through chemical adsorption. The Y(III) adsorption stabilities for the three activated carbon structures (C, C I, and C II) decreased in the order C I > C II > C.

4. Conclusions

This study used *Camellia oleifera* shells as the precursor and prepared activated carbon *via* phosphoric acid activation. The effects of the particle sizes, impregnation times, impregnation ratios, and activation temperatures on the adsorption of Y(III) were investigated. The activated carbon from the COS showed significant adsorption capacity and great potential for use in rare earth ion recovery. The kinetic studies indicated that adsorption occurred *via* monolayer adsorption and chemical adsorption. The SEM-EDS data indicated that Y(III) was stably adsorbed on the surface of the activated carbon from the COS. The mechanism for adsorption of Y(III) on the surface of the activated carbon was studied through first principles calculations, which showed that Y(III) interacted with carbon atoms on the surfaces of C, C I, and C II to form new chemical bonds. The calculated adsorption energies shows that the stabilities for Y(III) adsorption on the three different activated carbons decreased in the order C I > C II > C. This work provides an inexpensive and efficient adsorbent for environmentally friendly recovery of rare earth Y(III) waste from dilute solutions.

Data availability

Data will be made available on request.

Author contributions

Bin Zeng: conceptualization, methodology, investigation, data curation, writing – original draft. Xiangrong Zeng: conceptualization, methodology, investigation, writing – original draft, writing—review and editing. Lianghui Hu: investigation, data curation. Lijinhong Huang: investigation, data curation, writing—review and editing, funding acquisition. Yuxiang Huang: investigation, data curation. Yi Zhou: investigation, data curation. Guoliang Liu: investigation, data curation. Wanfu Huang: data curation, conceptualization, supervision, funding acquisition.

Conflicts of interest

The authors declare that they have no known competing financial interests or personal relationships that could have appeared to influence the work reported in this paper.

Acknowledgements

This work is financially supported by National Natural Science Foundation of China (Number: 51864017), The Support of the High Level and Skilled Talents Training Project of Jiangxi Province, Jiangxi Province Key R&D Plan "Unveiling and Leading" Project "New Technology and Application Demonstration for Efficient Resource Utilization of Low Grade Complex Tungsten and Molybdenum Mines" (Number: 20223BBH80012).

References

1 A. Turner, J. W. Scott and L. A. Green, Rare earth elements in plastics, *Sci. Total Environ.*, 2021, **774**, 145405.
2 X. Yang, P. L. Rozelle and S. V. Pisupati, The effect of caustic soda treatment to recover rare earth elements from secondary feedstocks with low concentrations, *Miner. Eng.*, 2021, **173**, 107184.
3 Q. Wang, H. Fan, Y. Xiao and Y. Zhang, Applications and recent advances of rare earth in solid oxide fuel cells, *J. Rare Earths*, 2022, **40**(11), 1668–1681.
4 X. Guan, P. Li, W. Liu, Q. Chang, Y. Han, J. Zhang, H. Zhang, Q. Li and S. Zheng, Adsorption mechanism of yttrium ions

onto ion-adsorption type rare earths ore, *Sep. Purif. Technol.*, 2022, **299**, 121641.

5 Y. Liu, K. Hu, X. Zhou, C. Zhang, F. Gao, X. Li and Y. Wan, Transformation of YF3 into Y(OH)3 by a Mechanochemical Process: Extracting Yttrium from Rare Earth Smelting Slag under Mild Conditions, *ACS Sustain. Chem. Eng.*, 2023, **11**(13), 4969–4979.

6 M. Malekan, R. Rashidi, M. Bozorg and N. Birbilis, Tailoring the glass forming ability, mechanical properties and corrosion resistance of Cu–Zr–Al bulk metallic glasses by yttrium addition, *Intermetallics*, 2023, **158**, 107906.

7 S. Wang, Y. Wang, Q. M. Ramasse, R. Schmid-Fetzer and Z. Fan, Segregation of Yttrium at the Mg/MgO interface in an Mg-0.5Y Alloy, *Acta Mater.*, 2023, **257**, 119147.

8 G. Wu, Z. Zhang, Y. Li and W. Liao, Extraction and separation of yttrium from other rare earths in chloride medium by phosphorylcarboxylic acids, *J. Rare Earths*, 2022, **40**(6), 958–964.

9 X. Li, W. Qiao, D. Chen, P. Wu, Y. Xie and X. Chen, Anomalous concentrations of rare earth elements in acid mine drainage and implications for rare earth resources from late Permian coal seams in northern Guizhou, *Sci. Total Environ.*, 2023, **879**, 163051.

10 L. Lefticariu, K. L. Klitzing and A. Kolker, Rare Earth Elements and Yttrium (REY) in coal mine drainage from the Illinois Basin, USA, *Int. J. Coal Geol.*, 2020, **217**, 103327.

11 X. Li, X. Ma, S. Ye, J. Wang, Y. Chen and C. Zhong, Potentiality of low-temperature carbides from excess sludge to recover low-concentration rare earth ions: Isotherm, kinetic and thermodynamic, *Chem. Eng. Res. Des.*, 2023, **193**, 168–178.

12 H. Singer, R. Steudtner, I. Sottorff, B. Drobot, A. Pol, H. J. M. Op den Camp and L. J. Daumann, Learning from nature: recovery of rare earth elements by the extremophilic bacterium Methylacidiphilum fumariolicum, *Chem. Commun.*, 2023, **59**(59), 9066–9069.

13 X. Meng, H. Zhao, Y. Zhao, L. Shen, G. Gu and G. Qiu, Effective recovery of rare earth from (bio)leaching solution through precipitation of rare earth-citrate complex, *Water Res.*, 2023, **233**, 119752.

14 Y. Li, Y. Wang, S. Kuang and W. Liao, Separation of rare earths in chloride media by synergistic solvent extraction with mixture of HEHAMP and CA12 and stripping with HCl, *Hydrometallurgy*, 2022, **213**, 105912.

15 M. M. Rahman, M. R. Awual and A. M. Asiri, Preparation and evaluation of composite hybrid nanomaterials for rare-earth elements separation and recovery, *Sep. Purif. Technol.*, 2020, **253**, 117515.

16 D. Saha, V. Bhasin, S. Khalid, N. Smeriglio, S. Cuka, D. Bhattacharyya, J. Rodgers, P. Panja, M. Deo and T. Apple, Adsorption of rare earth elements in carboxylated mesoporous carbon, *Sep. Purif. Technol.*, 2023, **314**, 123583.

17 D. Comandella, W. Bonani, J. B. Ciscar, J. Ponti, M. Cologna, K. Popa and D. Gilliland, Recovery of rare earth elements by nanometric CeO(2) embedded into electrospun PVA nanofibres, *RSC Adv.*, 2021, **11**(32), 19351–19362.

18 B. Lapo, J. J. Bou, J. Hoyo, M. Carrillo, K. Pena, T. Tzanov and A. M. Sastre, A potential lignocellulosic biomass based on banana waste for critical rare earths recovery from aqueous solutions, *Environ. Pollut.*, 2020, **264**, 114409.

19 E. M. Iannicelli-Zubiani, C. Cristiani, G. Dotelli, P. Gallo Stampino, R. Pelosato, E. Mesto, E. Schingaro and M. Lacalamita, Use of natural clays as sorbent materials for rare earth ions: Materials characterization and set up of the operative parameters, *Waste Manag.*, 2015, **46**, 546–556.

20 C. Cristiani, E. M. Iannicelli-Zubiani, M. Bellotto, G. Dotelli, P. G. Stampino, S. Latorrata, G. Ramis and E. Finocchio, Capture Mechanism of La and Cu Ions in Mixed Solutions by Clay and Organoclay, *Ind. Eng. Chem. Res.*, 2021, **60**(18), 6803–6813.

21 J. Liu, L. Zeng, S. Liao, X. Liao, J. Liu, J. Mao, Y. Chen, T. Qiu and S. Ren, Highly efficient enrichment and adsorption of rare earth ions (yttrium(III)) by recyclable magnetic nitrogen functionalized mesoporous expanded perlite, *Chin. Chem. Lett.*, 2020, **31**(10), 2849–2853.

22 M. Hermassi, M. Granados, C. Valderrama, C. Ayora and J. L. Cortina, Recovery of rare earth elements from acidic mine waters: An unknown secondary resource, *Sci. Total Environ.*, 2022, **810**, 152258.

23 K. C. Chaydarreh, X. Lin, L. Guan, H. Yun, J. Gu and C. Hu, Utilization of tea oil camellia (Camellia oleifera Abel.) shells as alternative raw materials for manufacturing particleboard, *Ind. Crops Prod.*, 2021, **161**, 113221.

24 W. Xu, W. Zhang, M. Han, F. Zhang, F. Lei, X. Cheng, R. Ning, K. Wang, L. Ji and J. Jiang, Production of xylooligosaccharides from Camellia oleifera Abel fruit shell using a shell-based solid acid catalyst, *Bioresour. Technol.*, 2022, **365**, 128173.

25 X. Liu, M. Xie, Y. Hu, S. Li, S. Nie, A. Zhang, H. Wu, C. Li, Z. Xiao and C. Hu, Facile preparation of lignin nanoparticles from waste Camellia oleifera shell: The solvent effect on the structural characteristic of lignin nanoparticles, *Ind. Crops Prod.*, 2022, **183**, 114943.

26 L. Huang, H. Peng, Z. Xiao, H. Wu, G. Fu, Y. Wan and H. Bi, Production of furfural and 5-hydroxymethyl furfural from Camellia oleifera fruit shell in [Bmim]HSO4/H2O/1,4-dioxane biphasic medium, *Ind. Crops Prod.*, 2022, **184**, 115006.

27 X. Liu, W. Meng, S. Cheng, B. Xing, Y. Zheng, X. Ren, M. Xue, C. Zhang and H. Xia, Utilization of camellia oleifera shell for production of valuable products by pyrolysis, *Arabian J. Chem.*, 2022, **15**(12), 104348.

28 R. Ning, X. Cheng, F. Zhang, D. Chen, W. Li, L. Zhang, L. Zhu and J. Jiang, Comparative study on potentials of Camellia oleifera shell saponins as foam cleaning agents in the late growth stage, *J. Cleaner Prod.*, 2023, **420**, 138326.

29 H. Long, J. Gu, J. Jiang, L. Guan, X. Lin, W. Zhang and C. Hu, Mechanically strong and biodegradable holocellulose films prepared from Camellia oleifera shells, *Carbohydr. Polym.*, 2023, **299**, 120189.

30 L. Mei, H. Qiao, F. Ke, C. Peng, R. Hou, X. Wan and H. Cai, One-step synthesis of zirconium dioxide-biochar derived

from Camellia oleifera seed shell with enhanced removal capacity for fluoride from water, *Appl. Surf. Sci.*, 2020, **509**, 144685.

31 H. Guo, C. Bi, C. Zeng, W. Ma, L. Yan, K. Li and K. Wei, Camellia oleifera seed shell carbon as an efficient renewable bio-adsorbent for the adsorption removal of hexavalent chromium and methylene blue from aqueous solution, *J. Mol. Liq.*, 2018, **249**, 629–636.

32 Q. Liu, D. Li, H. Cheng, J. Cheng, K. Du, Y. Hu and Y. Chen, High mesoporosity phosphorus-containing biochar fabricated from Camellia oleifera shells: Impressive tetracycline adsorption performance and promotion of pyrophosphate-like surface functional groups (C-O-P bond), *Bioresour. Technol.*, 2021, **329**, 124922.

33 Y. Fan, H. Wang, L. Deng, Y. Wang, D. Kang, C. Li and H. Chen, Enhanced adsorption of Pb(II) by nitrogen and phosphorus co-doped biochar derived from Camellia oleifera shells, *Environ. Res.*, 2020, **191**, 110030.

34 L. Dong, L. Hou, Z. Wang, P. Gu, G. Chen and R. Jiang, A new function of spent activated carbon in BAC process: Removing heavy metals by ion exchange mechanism, *J. Hazard. Mater.*, 2018, **359**, 76–84.

35 F.-C. Wu, R.-L. Tseng and R.-S. Juang, Characteristics of Elovich equation used for the analysis of adsorption kinetics in dye-chitosan systems, *Chem. Eng. J.*, 2009, **150**(2–3), 366–373.

36 E. Kusrini, W. Wicaksono, C. Gunawan, N. Z. A. Daud and A. Usman, Kinetics, mechanism, and thermodynamics of lanthanum adsorption on pectin extracted from durian rind, *J. Environ. Chem. Eng.*, 2018, **6**(5), 6580–6588.

37 L. A. Attia and R. Gamal, Fabrication of cobalt iron oxide alginate nanocomposite as an eco-friendly sorbent for Y(III) and Sr(II) removal from aqueous solution, *J. Mol. Liq.*, 2023, **369**, 120856.

38 S. Su, B. Chen, M. He, B. Hu and Z. Xiao, Determination of trace/ultratrace rare earth elements in environmental samples by ICP-MS after magnetic solid phase extraction with Fe3O4@SiO2@polyaniline–graphene oxide composite, *Talanta*, 2014, **119**, 458–466.

39 X. Zhao, X. Jiang, D. Peng, J. Teng and J. Yu, Behavior and mechanism of graphene oxide-tris(4-aminophenyl)amine composites in adsorption of rare earth elements, *J. Rare Earths*, 2021, **39**, 90–97.

40 P. Yan, M. He, B. Chen and B. Hu, Fast preconcentration of trace rare earth elements from environmental samples by di(2-ethylhexyl)phosphoric acid grafted magnetic nanoparticles followed by inductively coupled plasma mass spectrometry detection, *Spectrochim. Acta, Part B*, 2017, **136**, 73–80.

41 P. Liang, B. Hu, Z. Jiang, Y. Qin and T. Peng, Nanometer-sized titanium dioxide micro-column on-line preconcentration of La, Y, Yb, Eu, Dy and their determination by inductively coupled plasma atomic emission spectrometry, *J. Anal. At. Spectrom.*, 2001, **16**(no. 8), 863–866.

42 Q. Li, W. Xu, X. Liang, B. Liu, Q. Wu, Z. Zeng, L. Li and X. Ma, Specific alkali metal sites as CO2 traps in activated carbon with different pore size for CO2 selective adsorption: GCMC and DFT simulations, *Fuel*, 2022, **325**, 124871.

43 Q. Lyu, Y. Liu, Y. Guan, X. Liu and D. Che, DFT study on the mechanisms of mercury removal from natural gas over Se-modified activated carbon, *Fuel*, 2022, **324**, 124658.

44 N. Chen and R. T. Yang, Ab initio molecular orbital calculation on graphite: selection of molecular system and model chemistry, *Carbon*, 1998, **36**(no. 7), 1061–1070.

45 W. Cheng and C. Wan, Waste to wealth: Oxygen-nitrogen-sulfur codoped lignin-derived carbon microspheres from hazardous black liquors for high-performance DSSCs, *J. Energy Chem.*, 2023, **83**, 549–563.